

Article

Enhancing the High-Temperature Strength of a Co-Base Superalloy by Optimizing the γ/γ' Microstructure

D. Hausmann ^{1,*}, C. Solís ² , L.P. Freund ¹, N. Volz ¹, A. Heinemann ², M. Göken ¹, R. Gilles ² and S. Neumeier ¹ 

¹ Department of Materials Science and Engineering, Friedrich-Alexander-Universität Erlangen-Nürnberg, 91058 Erlangen, Germany; lisa.freund@fau.de (L.P.F.); nicklas.volz@fau.de (N.V.); mathias.goeken@fau.de (M.G.); steffen.neumeier@fau.de (S.N.)

² Heinz Maier-Leibnitz Zentrum, Technische Universität München, 85748 Garching, Germany; Cecilia.Solis@frm2.tum.de (C.S.); andre.heinemann@hzg.de (A.H.); ralph.gilles@tum.de (R.G.)

* Correspondence: daniel.dh.hausmann@fau.de; Tel.: +49-9131-85-27478

Received: 31 January 2020; Accepted: 25 February 2020; Published: 28 February 2020



Abstract: Compositionally complex polycrystalline γ/γ' CoNi-base superalloys, such as CoWAlloy2 (Co41-Ni32-Cr12-Al9-W5-Ti0.3-Ta0.2-Si0.4-Hf0.1-C-B-Zr) are interesting candidates for new high-temperature materials. To maximize their high-temperature strength, the γ/γ' microstructure has to be optimized by adjusting the multi-step heat treatments. Various microstructures after different heat treatments were analyzed by scanning and transmission electron microscopy and especially in-situ small-angle neutron scattering during heat treatment experiments. The corresponding mechanical properties were determined by compression tests and hardness measurements. From this, an optimum γ' precipitate size was determined that is adjusted mainly in the first precipitation heat treatment step. This is discussed on the basis of the theory of shearing of γ' precipitates by weak and strong pair-couplings of dislocations. A second age hardening step leads to a further increase in the γ' volume fraction above 70% and the formation of tertiary γ' precipitates in the γ channels, resulting in an increased hardness and yield strength. A comparison between two different three-step heat treatments revealed an increase in strength of 75 MPa for the optimized heat treatment.

Keywords: compositionally complex alloy; CoNi-base superalloy; scanning electron microscopy transmission; electron microscopy; small-angle neutron scattering; precipitation behavior; hardness; yield stress

1. Introduction

In recent years, different compositionally complex, γ' -strengthened CoNi-base superalloys in the Co–Al–W system were developed [1–6]. Investigations revealed that, in particular, the polycrystalline CoNi-base superalloys are promising for high-temperature applications [1,7]. Compared to the alloys of the simple ternary and quaternary Co–Al–W–X systems, the polycrystalline alloys of the CoWAlloy series exhibited an improved oxidation behavior [8,9] and enhanced mechanical properties [1,2,7]. A large gap between solidus and γ' solvus temperature together with a high γ' volume fraction is regarded to be beneficial for the usage as wrought alloys. After a three-step recrystallization and aging heat treatment, the L1₂ ordered γ' (Co, Ni)₃(Al, W, Ti, Ta) phase is precipitated in a multimodal distribution of particle size of large primary, smaller secondary, and ternary precipitates that are coherently embedded in the γ matrix phase. The primary γ' precipitates emerge during deformation and the recrystallization heat treatment. Secondary and tertiary γ' precipitates occur during the aging heat treatment. Previous microstructural investigations on the alloy CoWAlloy2 revealed that the γ'

volume fraction of the secondary γ' precipitates is slightly above 50% and the diameter of the primary and secondary γ' precipitates is of about 0.2 μm and 60 nm [1,10]. Comparable cast and wrought Ni-base superalloys, such as Waspaloy and U720Li, have total γ' volume fractions below 50%.

From Ni-base superalloys, it is known that the precipitation strengthening mechanisms depend on the volume fraction and size of these precipitates. To predict the precipitation strengthening contribution and to adjust the optimum γ' precipitate size, the model for weak and strong pair-couplings of dislocations is used [11,12]. Typically, dislocations travel in pairs. While the leading partial dislocation encounters an obstacle and creates an anti-phase boundary (APB), the following partial dislocation restores the original order. If the precipitates are smaller than a critical particle size, the pair of partial dislocations is weakly coupled, i.e., the leading and the trailing dislocations are cutting different precipitates. Precipitates that are larger than a critical particle size lead to strong pair-coupling. The coupled dislocation pair is in the same precipitate. At the transition between weak and strong pair-coupling, it can be expected that the material reaches a maximum of strength and hardness.

In order to achieve the highest possible mechanical strength of the developed CoNi-base superalloys, also the γ/γ' microstructure has to be optimized by adjusting the multi-step heat treatment procedures. However, it is not clear whether the model of weak and strong-pair coupling can be used for CoNi-base superalloys, too, and what the optimum γ/γ' microstructure is and how large the total γ' volume fractions are. So far, the deformation mechanisms at strain rates of 10^{-4} s^{-1} or faster have not been investigated yet. Previous investigations on the creep deformation mechanisms of single crystalline γ/γ' CoNi-base superalloys at lower strain rates revealed that the shearing of the γ' phase occurs by forming APB/SISF/APB configurations at 900 °C [3] or by forming APB/SISF/APB configurations and later by SISFs at 850 °C (SISF: Superlattice intrinsic stacking fault). Other polycrystalline γ/γ' CoNi-base superalloys showed that the γ' precipitates are sheared by $a/6 \langle 112 \rangle$ Shockley partial dislocations and microtwins are formed during creep at 750 °C [13].

In this study, different heat treatment strategies were performed to adjust the microstructure and consequently improve the high-temperature mechanical properties of the polycrystalline γ/γ' CoNi-base superalloy CoWAlloy2. To reveal the correlation between microstructure and mechanical properties, the different conditions were characterized in detail by scanning electron microscopy (SEM), transmission electron microscopy (TEM), hardness measurements, and compression tests. Complementary in-situ and ex-situ small-angle neutron scattering (SANS) investigations were performed to get representative information from larger volumes about the temporal evolution of the γ' precipitate phase. Previous studies demonstrated that two-phase superalloys can be successfully analyzed by SANS to investigate the microstructural evolution of the γ/γ' microstructure during heat treatments [14–18]. In this study, the γ' precipitate size distributions and volume fractions during the heat treatment procedures and after the full three-step heat treatment were determined quantitatively. The goal was to find the optimum γ/γ' microstructure and to check whether the existing precipitation strengthening models can be applied for these novel γ/γ' CoNi-base superalloys.

2. Materials and Methods

Table 1 gives the elemental composition of the investigated alloy named CoWAlloy2.

Table 1. Nominal alloy composition of CoWAlloy2 in at.%.

Element	Co	Ni	Cr	Al	W	Ti	Ta	Si	Zr	Hf	B	C
CoWAlloy2	40.8	32.0	12.0	9.0	5.0	0.3	0.2	0.4	0.01	0.1	0.08	0.08

The alloy was vacuum arc melted from raw elements, cast and homogenized for 3 h at 1250 °C in air. Bars of the material with an initial diameter of 40 mm were rolled in several steps down to a diameter of 15 mm on a non-heated rolling mill with a starting temperature of 1100 °C at the company Vacuumschmelze GmbH (Hanau, Germany). To recrystallize the rolled bar, a subsequent heat treatment (4 h/1000 °C, oil quenched) was applied. After recrystallization (as-RX), the material

was cut into about 2 mm thick slices and quartered. Several annealing heat treatments were performed in air to produce different γ' distributions. The first aging heat treatment step was performed at 800 °C and 900 °C for 2, 4, 8, and 16 h (step I). All samples were air cooled after the individual heat treatment steps. Based on the results found, a second aging heat treatment step was added to promote the growth of tertiary γ' precipitates and to further increase the γ' volume fraction (step II). This additional heat treatment was performed at 725 °C or 750 °C for 16 h on samples annealed at 800 °C or 900 °C for 4 h. All samples were air cooled after the individual heat treatment steps. The heat treatment procedure is based on Waspaloy [19].

The microstructures were investigated by using a SEM Zeiss Crossbeam (Zeiss, Oberkochen, Germany) 1540 EsB in conjunction with a back-scattered electron detector and an acceleration voltage of 20 kV at 7 mm working distance. The samples were cut, ground, and polished up to 1 μm , and in a final step, polished with colloidal silica. For TEM investigations, 200 μm thick slices with a diameter of 3 mm were prepared. Electrolytic thinning of the samples was done with a 6 vol.% perchloric acid solution in methanol at about -25 °C with a Struers Double Jet Tenupol-5 (Struers, Willich, Germany). TEM investigations were performed on a Philips CM 200 (Philips, Amsterdam, Netherlands) operated at 200 kV.

The mechanical properties after the different heat treatments were assessed by Vickers hardness testing with a load of 98.1 N. For the two-step heat treatments, compression tests were additionally performed on cylindrical samples. The samples with a diameter of 3 mm and a length of 4.5 mm were manufactured by wire spark erosion and ground to achieve parallel surfaces. The compression tests were performed on an electromechanical Instron 4505 testing machine (Instron, Norwood, MA, USA) at room temperature (RT), 600 °C, 750 °C, 800 °C, and 850 °C with a strain rate of 10^{-4} s $^{-1}$. At least three tests were conducted at each temperature.

Since the determination of the γ' particle size distribution and γ' volume fraction of the complex tridisperse γ' structure is difficult by electron microscopy techniques, in-situ and ex-situ heat treatments were performed at the small-angle neutron scattering facility SANS-1 at the Heinz-Maier-Leibnitz Center of the TU München (FRM II) [20]. For the SANS measurements, discs with a diameter of 15 mm were cut from recrystallized bars in fully heat-treated conditions, which were ground to achieve parallel surfaces and a thickness of 1 mm. A high-temperature vacuum furnace was implemented in the beam line. To cover a maximum q-range (range of scattering angles for determination of the precipitate size distribution), data from three detector configurations were measured and combined to produce one SANS spectrum. The detector distance was varied between 2 m, 8 m, and 20 m. The scattering measurement was performed with a beam diameter of 8 mm and a wave length of 6 Å at the lower detector distances and 12 Å at the detector distance of 20 m. To reproduce the heat treatment procedure, the recrystallized samples were characterized in-situ at room temperature first and then at the first heat treatment temperature at 800 °C or 900 °C, respectively. Each measurement lasted for about 1 h, so the total annealing time at 800 °C or 900 °C was about 2 h. In addition to that, ex-situ measurements of the fully heat-treated conditions were performed. Afterwards the scattering patterns were analyzed, calibrated with water measurements and merged with the software BerSANS [21]. The SASFit program [22] was used for fitting the corrected data in which the γ' hardening precipitates were modeled as spherical particles with a log-normal distributed particle size. To calculate the scattering factors of the secondary and tertiary γ' and the surrounding γ matrix phase, their chemical compositions were used, which were determined by atom probe tomography (APT) in a previous study by Freund et al. [10]. Table 2 summarizes the compositions of the γ matrix and the γ' precipitates. The resulting scattering factor of the secondary γ' precipitates is 1.18×10^{10} cm $^{-2}$ and the scattering factor of the tertiary γ' precipitates was 9.08×10^9 cm 2 .

Table 2. Composition (at.%) of the secondary and tertiary γ' precipitates and the surrounding γ matrix phase of CoWAlloy2 determined by atom probe tomography (APT) [10].

	Co	Ni	Cr	Al	W	Ti	Ta	Si	Hf	B	C
γ matrix	49.0	21.3	20.9	3.6	4.4	0.04	0.03	0.64	0.02	0.013	0.008
	± 0.6	± 0.2	± 0.6	± 0.1	± 0.1	± 0.01	± 0.01	± 0.05	± 0.01	± 0.01	± 0.01
secondary γ'	32.8	39.4	5.4	14.5	6.1	0.50	0.37	0.35	0.14	0.025	0.006
	± 0.5	± 0.7	± 0.2	± 0.4	± 0.4	± 0.02	± 0.08	± 0.02	± 0.03	± 0.01	± 0.01
γ matrix	48.5	22.0	20.0	4.1	4.5	0.07	0.03	0.61	0.02	0.016	0.007
	± 2.4	± 2.9	± 2.5	± 1.5	± 0.4	± 0.08	± 0.03	± 0.09	± 0.01	± 0.01	± 0.01
tertiary γ'	34.9	38.2	5.4	12.5	7.4	0.44	0.19	0.38	0.06	0.011	0.008
	± 1.4	± 1.4	± 1.0	± 0.7	± 0.5	± 0.06	± 0.04	± 0.06	± 0.02	± 0.01	± 0.01

3. Results

3.1. Microstructural Characterization

3.1.1. Electron Microscopy

Various microstructures were generated by applying different heat treatments. The conditions after the recrystallization heat treatment (as-RX), after 4 h of the first aging step (step I), can be seen in Figure 1.

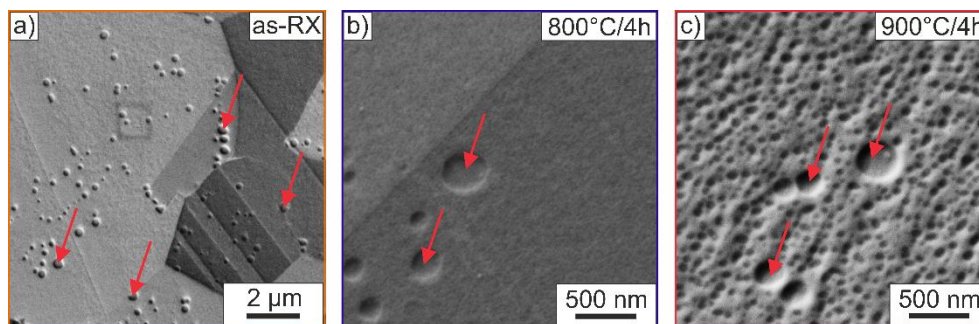


Figure 1. SEM images of different conditions: (a) as-RX; step I; (b) 800 °C/4 h and (c) 900 °C/4 h. The red arrows indicate the primary γ' precipitates.

The large primary γ' precipitates were characterized by SEM image analysis. They had a radius of about 150 nm formed during the recrystallization heat treatment at 1000 °C (see Figure 1a) since the γ' solvus temperature was 1030 °C [6]. These precipitates were distributed heterogeneously and their volume fraction was about 3%. During the first aging step at 800 °C, small secondary γ' precipitates emerged, which, however, were too small to be clearly seen in the SEM; see Figure 1b. In contrast, the secondary γ' precipitates after aging at 900 °C were coarsened to a radius of about 30 nm; see Figure 1c. The aging heat treatment step I primarily determined the size of the secondary γ' precipitates. In more detail, their temporal evolution between 2 h and 16 h of annealing at 800 °C and 900 °C was also examined using dark field TEM (see Figure 2).

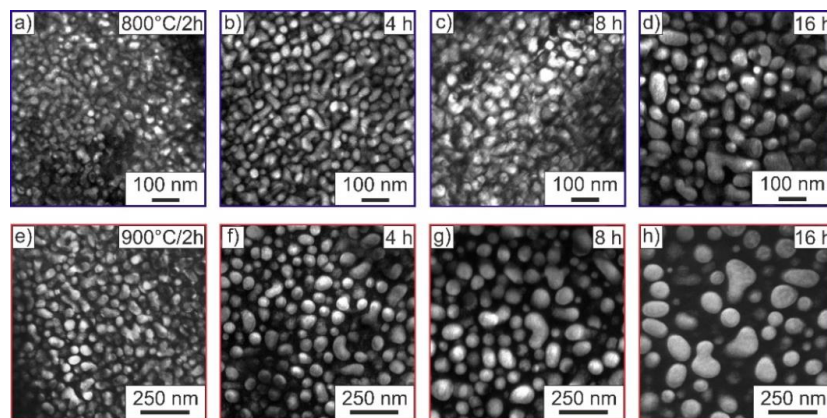


Figure 2. Dark field TEM images of the conditions after aging step I: (a) 2 h, (b) 4 h, (c) 8 h, and (d) 16 h at 800 °C; (e) 2 h, (f) 4 h, (g) 8 h, and (h) 16 h at 900 °C.

The size of the secondary γ' precipitates increased by increasing time and temperature of the annealing heat treatment (see Figure 2 and Table 3).

Table 3. Mean radius r of secondary γ' precipitates of the different conditions as determined by TEM.

Heat Treatment	800 °C				900 °C				800 °C/4 h +725 °C/16 h	900 °C/4 h +750 °C/16 h
	2	4	8	16	2	4	8	16		
Mean radius	10.3	12.8	14.6	19.6	21.4	26.4	34.2	45.2	19.4	36.1
sec. γ' /nm	± 2.0	± 2.6	± 4.5	± 4.0	± 7.2	± 6.5	± 8.8	± 13.5	± 6.4	± 7.0

In general, the γ' precipitates were nearly twice as big after annealing at 900 °C compared to 800 °C. By comparing the conditions after the first aging step and the full heat treatment, it can be seen that the bidisperse distribution of spherical γ' precipitates changed to a tridisperse one, but the size of the primary and secondary γ' precipitates stayed similar; see Figure 3.

The aging step II at 725 °C or 750 °C led mainly to a further increase of the γ' volume fraction by precipitation of very small tertiary γ' precipitates, which accumulated at the existing secondary γ' precipitates (Figure 3c) or formed in the γ matrix surrounding the secondary γ' precipitates (Figure 3d).

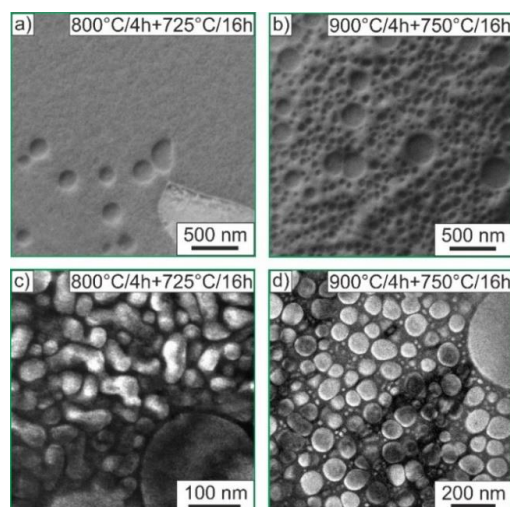


Figure 3. SEM images of the conditions after aging step II: (a) 800 °C/4 h + 725 °C/16 h and (b) 900 °C/4 h + 750 °C/16 h. Dark field TEM images of the conditions after aging step II: (c) 800 °C/4 h + 725 °C/16 h and (d) 900 °C/4 h + 750 °C/16 h.

3.1.2. Small-Angle Neutron Scattering

The absolute macroscopic scattering cross section $d\Sigma/d\Omega$ as a function of the scattering vector q of the fully heat-treated condition $900\text{ }^\circ\text{C}/4\text{ h} + 750\text{ }^\circ\text{C}/16\text{ h}$ is plotted exemplarily in Figure 4a.

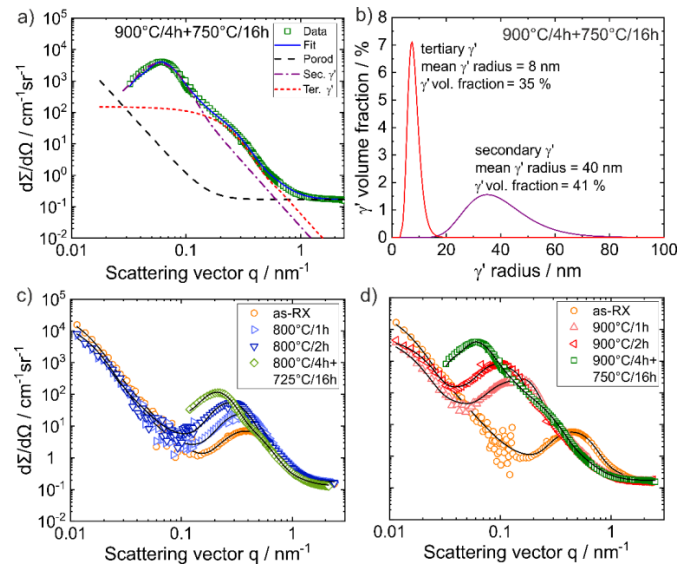


Figure 4. (a) Scattering curve of the condition $900\text{ }^\circ\text{C}/4\text{ h} + 750\text{ }^\circ\text{C}/16\text{ h}$ consisting of three different contributions: Log-normal size distributed secondary and tertiary γ' precipitates and a Porod signal; (b) the applied log-normal size distributions. Scattering curves of the different conditions: (c) as-RX, $800\text{ }^\circ\text{C}/1\text{ h}$, $800\text{ }^\circ\text{C}/2\text{ h}$ and $800\text{ }^\circ\text{C}/4\text{ h} + 725\text{ }^\circ\text{C}/16\text{ h}$ and (d) as-RX, $900\text{ }^\circ\text{C}/1\text{ h}$, $900\text{ }^\circ\text{C}/2\text{ h}$ and $900\text{ }^\circ\text{C}/4\text{ h} + 750\text{ }^\circ\text{C}/16\text{ h}$.

The measured data were fitted with a model of precipitates using a log-normal size distribution with secondary and tertiary γ' precipitates and the Porod signal, that leveled out in a constant incoherent background signal, yielded in the determined scattering curve. The corresponding applied log-normal size distributions of the precipitates are shown in Figure 4b.

The curve of the as-RX condition is shown as reference in Figure 4c,d, where only very small γ' precipitates, which formed during quenching, can be detected. The precipitates at $800\text{ }^\circ\text{C}$ after 1 h had a radius of about 5 nm and a volume fraction of about 51%. The scattering curves of the step I conditions revealed that the contribution coming from these small secondary γ' precipitates just shifted to lower values of the scattering vector q and the intensity contribution of the scattering signal increased with increasing temperature and time of the aging heat treatment. The increased scattering contribution indicates a higher γ' volume fraction and a lower value of the scattering vector q reveals a larger size of the precipitates.

With ongoing aging at $800\text{ }^\circ\text{C}$ the secondary γ' precipitates coarsened further. Additionally, some tertiary γ' precipitates were present. The total γ' volume fraction reached the relatively high level of 74% already after 1 h. At $900\text{ }^\circ\text{C}$, the secondary as well as tertiary γ' precipitates grew and reached a larger radius compared to the precipitates at $800\text{ }^\circ\text{C}$, whereas the volume fraction decreased and was about 51%. The fully heat-treated condition $800\text{ }^\circ\text{C}/4\text{ h} + 725\text{ }^\circ\text{C}/16\text{ h}$ had a slightly left-shifted scattering vector. That indicates a slightly increased size of the secondary and tertiary γ' precipitates compared to the step I condition at $800\text{ }^\circ\text{C}$. The γ' volume fraction of about 70% was in the same range as the condition after step I. The curve of the condition $900\text{ }^\circ\text{C}/4\text{ h} + 750\text{ }^\circ\text{C}/16\text{ h}$ was strongly shifted to a smaller scattering vector q and had a higher intensity contribution in contrast to the step I conditions at $900\text{ }^\circ\text{C}$. This resulted in sizes of tertiary γ' comparable to the $900\text{ }^\circ\text{C}$ step I conditions and into bigger secondary γ' precipitate sizes. In contrast to the step I conditions at $900\text{ }^\circ\text{C}$, the γ' volume fraction increased to about 76%. The summarized results of the measurements are shown in Table 4.

Table 4. Mean radius r and volume fraction f of secondary and tertiary γ' precipitates of the heat treatments as determined by small-angle neutron scattering (SANS). The width parameter σ represents the broadness of the γ' size distributions.

Condition	Secondary γ'			Tertiary γ'			Total γ'
	r/nm	σ/nm	$f/\%$	r/nm	σ/nm	$f/\%$	$f/\%$
as-RX	-	-	-	4.7	0.3	51	51
800 °C/1 h	7.0	0.3	41	3.7	0.5	33	74
800 °C/2 h	9.2	0.3	56	4.5	0.2	17	73
900 °C/1 h	18.3	0.3	39	7.2	0.4	12	51
900 °C/2 h	23.5	0.3	42	9.7	0.3	9	51
800 °C/4 h + 725 °C/16 h	12.2	0.3	49	5.6	0.2	21	70
900 °C/4 h + 750 °C/16 h	39.8	0.3	41	8.0	0.3	35	76

3.2. Mechanical Properties

Figure 5 shows the Vickers hardness in dependence of the heat treatment temperature and duration in comparison to the hardness of the as-RX condition.

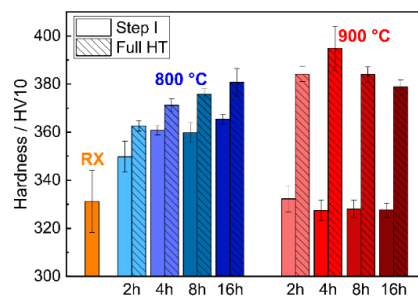


Figure 5. Vickers hardness in dependence of heat treatment temperature and duration after step I, i.e., aging at 800 °C or 900 °C and after the full heat treatment, i.e., step I + 750 °C/16 h.

It can be seen that the hardness after step I annealing at 800 °C increased continuously with longer heat treatment durations. At 900 °C, the different aging times led to very similar hardness values on a significantly lower level. The second annealing step caused a relatively small additional increase of the hardness compared to the condition that was aged at 800 °C, whereas the condition that was aged at 900 °C showed a larger increase of hardness. The fully heat-treated conditions that were aged in step I at 900 °C reached a maximum after 4 h. After 8 h and 16 h at 900 °C, the hardness decreased continuously, presumably due to over aging (see Discussion, chapter 4). Figure 6 shows the yield stress as a function of the test temperature after the full two-step heat treatment.

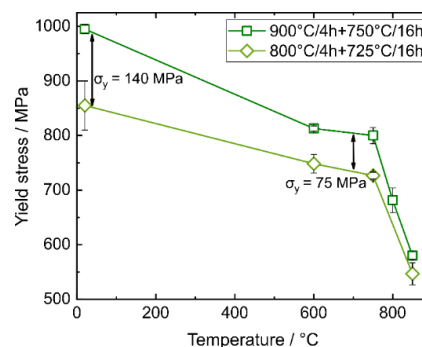


Figure 6. Yield stress under compression as a function of the testing temperature of two fully heat-treated conditions.

The yield stress decreased with increasing testing temperature with the heat treatment of 900 °C/4 h + 750 °C/16 h leading to the higher strength. The difference between both conditions varied from about 140 MPa at RT to about 75 MPa in the temperature regime from 600 °C to 800 °C. At higher temperatures, the difference diminished significantly.

4. Discussion

The size of the secondary γ' precipitates is adjusted predominantly in the first aging step, while the second aging step at lower temperatures mainly increases the γ' volume fraction. Therefore, the right aging temperature and time needs to be selected for step I. Figure 7 summarizes the SANS and TEM results on the evolution of the mean radius of the secondary γ' precipitates as a function of the annealing time.

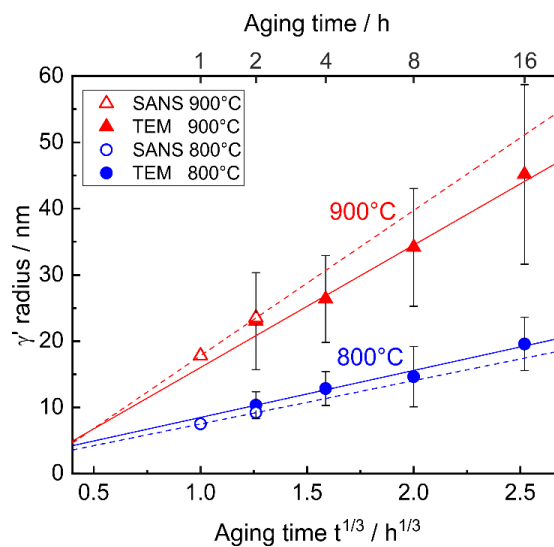


Figure 7. Mean radius of the secondary γ' precipitates as a function of the aging time for different aging temperatures, as determined by SANS and TEM.

The growth of the γ' precipitates can be described by the Lifshitz-Slyozov-Wagner theory. The γ' precipitate radius coarsens proportional to $\sqrt[3]{t}$. The results of the SANS measurements agree very well with the TEM investigations although the TEM data are generally slightly lower, which is well-known for TEM measurements of precipitate sizes [23]. It can be also seen that the size of the precipitates is larger and increases faster with higher annealing temperature due to the faster diffusion.

In order to understand the mechanical properties as determined by the Vickers hardness measurements, the theoretical strengthening contribution from the γ' precipitates with increasing precipitate radius was estimated according to the theory of cutting of γ' precipitates by weak or strong pair-coupled dislocations. The critical resolved shear stress (CRSS) for weak pair-coupling can be described by Equation (1) [24]:

$$\tau_{WP} = \frac{\gamma_{APB}}{2b} \left[\left(\frac{6\gamma_{APB}fr}{\pi T} \right)^{1/2} - f \right] \quad (1)$$

where γ_{APB} is the energy of an APB, b is the Burgers vector, f is the γ' volume fraction, and T is the line tension, which is approximately given as $\frac{1}{2}Gb^2$ with G as shear modulus. If the partial dislocation pair is strongly coupled and within the same precipitate, the CRSS is described by Equation (2) [24]:

$$\tau_{SP} = \sqrt{\frac{3}{2} \left(\frac{Gb}{r} \right) f^{1/2} \frac{w}{\pi^{3/2}} \left(\frac{2\pi\gamma_{APB}r}{wGb^2} - 1 \right)^{1/2}} \quad (2)$$

where w is a constant that is assumed as 1. An APB energy γ_{APB} of 155 mJ/m² [25], a shear modulus of 101 GPa [26], and a Burgers vector length of 0.253 nm, which is equivalent to the length of a $\frac{a}{2}$ 110 {111} dislocation that is based on the γ lattice parameter of 0.358 nm [27,28], were used for the calculation. A γ' volume fraction of 51% and 73%, which corresponds to the determined fractions at 800 °C and 900 °C, was assumed. The resulting correlations between the precipitation strengthening contributions and the γ' precipitate sizes are plotted in Figure 8.

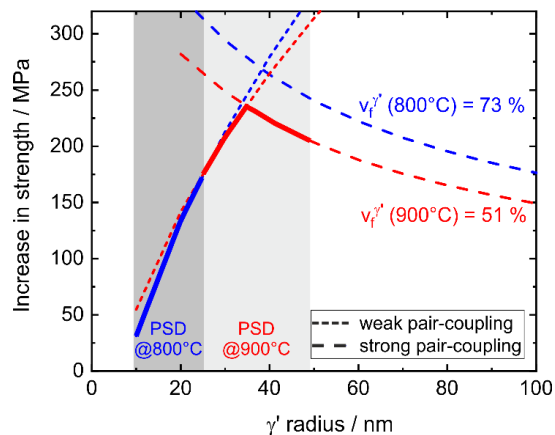


Figure 8. Dependence of the increase in strength on the mean radius of the γ' precipitates after the first aging step at 800 °C and 900 °C. The particle size distribution (PSD) of secondary γ' precipitates of the different conditions is marked.

The maximum strength is reached at a radius of about 34 nm, when the deformation mechanism changes from weak pair-coupling to strong pair-coupling according to the model. This explains why the hardness increases continuously as a function of the aging time at 800 °C (Figure 5). With increasing annealing time, the γ' precipitate size comes closer to the optimum size, but all conditions still represent underaged conditions. At 900 °C the hardness is on a similar level, because the γ' radii at the different annealing times range around the optimal γ' radius, which all lead to similar strengths. The reason for the higher hardness of all conditions that were aged at 800 °C compared to 900 °C in aging step I is the much higher γ' volume fraction of about 73% at 800 °C compared to about 51% at 900 °C; see Table 4.

This situation changes when the second aging step is conducted at 725 °C or 750 °C. This step II does not significantly further increase the γ' size and γ' volume fraction for the conditions that were aged at 800 °C in step I. Therefore, only a moderate further increase in hardness can be determined and the strength is not the highest since the secondary γ' precipitates remain underaged. However, the aging heat treatment step II causes a strong increase of the γ' volume fraction for the conditions that were aged at 900 °C in step I. The lower fraction of coarser secondary γ' precipitates at 900 °C leads to the nucleation of tertiary γ' precipitates in the γ matrix channels. Additionally, the secondary γ' precipitates are already close to the optimum precipitate size. As a consequence, the highest strength can be achieved for the heat treatment at 900 °C/4 h + 750 °C/16 h. The room temperature yield strength in this condition is 140 MPa higher for the other two-stage heat treatment at 800 °C/4 h + 725 °C/16 h. At 750 °C, a 75 MPa difference still persists.

5. Conclusions

The present study revealed how the γ/γ' microstructure of the CoNi-base superalloy CoWAlloy2 can be optimized to reach the maximum high temperature strength. The following conclusions can be drawn:

- A two-step aging heat treatment at 900 °C/4 h + 750 °C/16 h leads to the highest strength.
- The total γ' volume fraction is above 70%, as determined by SANS, which is exceptionally high for a wrought alloy.

- An optimum γ' precipitate size in the range of about 30–40 nm is found to reach the maximum strength, which can be explained by the model for weak and strong pair-coupling of dislocations.

Author Contributions: Conceptualization, S.N.; methodology, S.N.; investigation, D.H., L.F., N.V., A.H., R.G. and S.N.; data curation, C.S. and A.H.; writing—original draft preparation, D.H., L.F.; writing—review and editing, M.G., R.G., S.N.; project administration, S.N.; funding acquisition, M.G., R.G. and S.N. All authors have read and agreed to the published version of the manuscript.

Funding: This research received no external funding.

Acknowledgments: The authors acknowledge the funding support by the Federal Ministry of Education and Research (BMBF) through the project “An innovative testing machine for heating, quenching, tension, compression and cracking studies of industrial relevant high-temperature alloys—HiMat” (project number 05K19WEC and 05K19WO7).

Conflicts of Interest: The authors declare no conflict of interest.

References

1. Neumeier, S.; Freund, L.P.; Göken, M. Novel wrought γ/γ' cobalt base superalloys with high strength and improved oxidation resistance. *Scr. Mater.* **2015**, *109*, 104–107. [[CrossRef](#)]
2. Knop, M.; Mulvey, P.; Ismail, F.; Radecka, A.; Rahman, K.M.; Lindley, T.C.; Shollock, B.A.; Hardy, M.C.; Moody, M.P.; Martin, T.L.; et al. A New Polycrystalline Co-Ni Superalloy. *JOM* **2014**, *66*, 2495–2501. [[CrossRef](#)]
3. Titus, M.S.; Eggeler, Y.M.; Suzuki, A.; Pollock, T.M. Creep-induced planar defects in L1₂-containing Co- and CoNi-base single-crystal superalloys. *Acta Mater.* **2015**, *82*, 530–539. [[CrossRef](#)]
4. Lass, E.A.; Williams, M.E.; Campbell, C.E.; Moon, K.-W.; Kattner, U.R. γ' Phase Stability and Phase Equilibrium in Ternary Co-Al-W at 900°. *J. Phase Equilibria Diffus.* **2014**, *35*, 711–723. [[CrossRef](#)]
5. Lass, E.A.; Sauza, D.J.; Dunand, D.C.; Seidman, D.N. Multicomponent γ' -strengthened Co-based superalloys with increased solvus temperatures and reduced mass density. *Acta Mater.* **2018**, *147*, 284–295. [[CrossRef](#)]
6. Sani, S.A.; Arabi, H.; Kheirandish, S.; Ebrahimi, G. Investigation on the homogenization treatment and element segregation on the microstructure of a γ/γ' -cobalt-based superalloy. *Int. J. Miner. Metall. Mater.* **2019**, *26*, 222–233. [[CrossRef](#)]
7. Freund, L.P.; Giese, S.; Schwimmer, D.; Höppel, H.W.; Neumeier, S.; Göken, M. High temperature properties and fatigue strength of novel wrought γ/γ' Co-base superalloys. *J. Mater. Res.* **2017**, *32*, 4475–4482. [[CrossRef](#)]
8. Klein, L.; Shen, Y.; Killian, M.S.; Virtanen, S. Effect of B and Cr on the high temperature oxidation behaviour of novel γ/γ' -strengthened Co-base superalloys. *Corros. Sci.* **2011**, *53*, 2713–2720. [[CrossRef](#)]
9. Yan, H.-Y.; Vorontsov, V.A.; Dye, D. Effect of alloying on the oxidation behaviour of Co–Al–W superalloys. *Corros. Sci.* **2014**, *83*, 382–395. [[CrossRef](#)]
10. Freund, L.P.; Stark, A.; Pyczak, F.; Schell, N.; Göken, M.; Neumeier, S. The grain boundary pinning effect of the μ phase in an advanced polycrystalline γ/γ' Co-base superalloy. *J. Alloys Compd.* **2018**, *753*, 333–342. [[CrossRef](#)]
11. Kozar, R.W.; Suzuki, A.; Milligan, W.W.; Schirra, J.J.; Savage, M.F.; Pollock, T.M. Strengthening Mechanisms in Polycrystalline Multimodal Nickel-Base Superalloys. *Metall. Mater. Trans. A* **2009**, *40*, 1588–1603. [[CrossRef](#)]
12. Galindo-Nava, E.I.; Connor, L.D.; Rae, C.M.F. On the prediction of the yield stress of unimodal and multimodal γ' Nickel-base superalloys. *Acta Mater.* **2015**, *98*, 377–390. [[CrossRef](#)]
13. Freund, L.P.; Messé, O.M.D.M.; Barnard, J.S.; Göken, M.; Neumeier, S.; Rae, C.M.F. Segregation assisted microtwinning during creep of a polycrystalline L1₂-hardened Co-base superalloy. *Acta Mater.* **2017**, *123*, 295–304. [[CrossRef](#)]
14. Gilles, R.; Mukherji, D.; Eckerlebe, H.; Strunz, P.; Rösler, J. In Situ Investigation with Neutrons on the Evolution of γ' Precipitates at High Temperatures in a Single Crystal Ni-Base Superalloy. *Adv. Mater. Res.* **2011**, *278*, 42–47. [[CrossRef](#)]
15. Collins, D.M.; Heenan, R.K.; Stone, H.J. Characterization of Gamma Prime γ' precipitates in a Polycrystalline Nickel-Base Superalloy Using Small-Angle Neutron Scattering. *Metall. Mater. Trans. A* **2011**, *42*, 49–59. [[CrossRef](#)]

16. del Genovese, D.; Rösler, J.; Strunz, P.; Mukherji, D.; Gilles, R. Microstructural characterization of a modified 706-type Ni-Fe superalloy by small-angle neutron scattering and electron microscopy. *Metall. Mater. Trans. A* **2005**, *36*, 3439–3450. [[CrossRef](#)]
17. Mukherji, D.; del Genovese, D.; Strunz, P.; Gilles, R.; Wiedenmann, A.; Rösler, J. Microstructural characterisation of a Ni-Fe-based superalloy by in situ small-angle neutron scattering measurements. *J. Phys. Condens. Matter* **2008**, *20*, 104220. [[CrossRef](#)]
18. Ratel, N.; Bruno, G.; Demé, B. In situ small-angle neutron scattering investigation of the γ' precipitation and growth in the nickel-based single-crystal alloy SC16. *J. Phys. Condens. Matter* **2005**, *17*, 7061–7075. [[CrossRef](#)]
19. Byrne, J. Elevated temperature fatigue crack growth under dwell conditions in Waspaloy. *Int. J. Fatigue* **1997**, *19*, 359–367. [[CrossRef](#)]
20. Gilles, R.; Ostermann, A.; Schanzer, C.; Krimmer, B.; Petry, W. The concept of the new small-angle scattering instrument SANS-1 at the FRM-II. *Phys. B Condens. Matter* **2006**, *385–386*, 1174–1176. [[CrossRef](#)]
21. Keiderling, U. The new “BerSANS-PC” software for reduction and treatment of small angle neutron scattering data. *Appl. Phys. A: Mater. Sci. Process.* **2002**, *74*, 1455–1457. [[CrossRef](#)]
22. Breßler, I.; Kohlbrecher, J.; Thünemann, A.F. SASfit: A tool for small-angle scattering data analysis using a library of analytical expressions. *J. Appl. Crystallogr.* **2015**, *48*, 1587–1598. [[CrossRef](#)] [[PubMed](#)]
23. Gilles, R.; Mukherji, D.; Karge, L.; Strunz, P.; Beran, P.; Barbier, B.; Kriele, A.; Hofmann, M.; Eckerlebe, H.; Rösler, J. Stability of TaC precipitates in a Co-Re-based alloy being developed for ultra-high-temperature applications. *J. Appl. Crystallogr.* **2016**, *49*, 1253–1265. [[CrossRef](#)]
24. Reed, R.C. *The Superalloys: Fundamentals and Applications*; Cambridge University Press: Cambridge, UK, 2006.
25. Okamoto, N.L.; Oohashi, T.; Adachi, H.; Kishida, K.; Inui, H.; Veyssi re, P. Plastic deformation of polycrystals of $\text{Co}_3(\text{Al,W})$ with the L_{12} structure. *Philos. Mag.* **2011**, *91*, 3667–3684. [[CrossRef](#)]
26. Tanaka, K.; Ohashi, T.; Kishida, K.; Inui, H. Single-crystal elastic constants of $\text{Co}_3(\text{Al,W})$ with the L_{12} structure. *Appl. Phys. Lett.* **2007**, *91*, 181907. [[CrossRef](#)]
27. Sato, J. Cobalt-Base High-Temperature Alloys. *Science* **2006**, *312*, 90–91. [[CrossRef](#)]
28. Bauer, A.; Neumeier, S.; Pyczak, F.; G oken, M. Creep strength and microstructure of polycrystalline γ' -strengthened Cobalt-base superalloys. In Proceedings of the Superalloys 2012: 12th International Symposium on Superalloys, Seven Springs Mountain Resort, Champion, PA, USA, 9–13 November 2012.



  2020 by the authors. Licensee MDPI, Basel, Switzerland. This article is an open access article distributed under the terms and conditions of the Creative Commons Attribution (CC BY) license (<http://creativecommons.org/licenses/by/4.0/>).